Characteristic of atmospheric mercury in the suburbs of East China: implication on sources and formation of mercury species over a regional transport intersection zone

Xiaofei Qin[1], Xiaohao Wang[2], Yijie Shi[1], Guangyuan Yu[1], Na Zhao[1], Yanfen Lin[2], Qingyan Fu[2], Dongfang Wang[2], Zhouqing Xie[3], Congrui Deng[1,*], Kan Huang[1,*]

[1]*Center for Atmospheric Chemistry Study, Shanghai Key Laboratory of Atmospheric Particle Pollution and Prevention (LAP[3]), Department of Environmental Science and Engineering, Fudan University, Shanghai, 200433 China*

[2]*Shanghai Environmental Monitoring Center, Shanghai, 200030 China*

[3]*School of Earth and Space Sciences, University of Science and Technology of China, Hefei, Anhui, 230026 China*

Correspondence: congruideng@fudan.edu.cn, huangkan@fudan.edu.cn

Abstract

Mercury (Hg) is a global pollutant of great concern in East Asia, which is considered to be the largest mercury-emitting region in the world. In this study, atmospheric gaseous elemental mercury (GEM), gaseous oxidized mercury (GOM), and particulate-bound mercury (PBM) were measured continuously over a regional transport intersection zone in the suburbs of East China to reveal the sources and formation of mercury species. The annual mean concentrations of GEM, PBM, and GOM reached 2.77 ng/m^3, 60.8 pg/m^3, and 82.1 pg/m^3, respectively. GEM concentrations were elevated in winter, summer, and spring while lower in autumn. This seasonal pattern of GEM suggested that the re-emissions from natural surfaces played a significant role in the fluctuation of atmospheric mercury in addition to anthropogenic sources. Relationship between Hg species and wind directions indicated the high Hg concentrations were related to winds from the south, southwest, and north of the measurement site. An application of the GOM/PBM tracer method and trajectory-based source region identification distinguished the relative importance of long-range transport from northern China and quasi-local emission sources on the magnitudes of Hg species. It was revealed that GEM concentrations were higher when quasi-local sources dominated compared

to the dominance of long-range transport events. Six sources and their contributions to anthropogenic GEM were identified. Besides the common anthropogenic emission sectors (i.e. industrial and biomass burning, coal combustion, iron and steel production, cement production, and incineration), shipping emission was found to be an important source (19.6%) of anthropogenic mercury in East China, where marine vessel shipping activities are intense. In addition, a considerable natural source of GEM was identified. Concurrences of high GOM concentrations with elevated O_3 and temperature, along with the lagged variation of GEM and GOM during daytime demonstrated the very high GOM concentrations were partially ascribed to the intense in situ oxidation of GEM. Statistical analysis showed that when $PM_{2.5}$ reached a certain threshold value, GOM was inhibited to some extent due to the gas-particle partitioning process. This process was controlled under the conditions of high $PM_{2.5}$ concentrations, high humidity, and low temperature.

1. Introduction

Mercury (Hg) is a global pollutant of great concerns for environment and human health. Based on its physical and chemical properties, atmospheric mercury is operationally divided into three forms, i.e. gaseous elemental mercury (GEM), particulate-bound mercury (PBM), and gaseous oxidized mercury (GOM). GEM is the predominant form in the atmosphere (>90%), while PBM consists of a small quantity of the total mercury as well as for GOM. Elemental mercury in the atmosphere is relatively stable, which means that it has a long lifetime of 0.5-2 year and can transport globally before they are oxidized and removed from the atmosphere via wet and dry depositions (Marsik et al., 2007). In contrast, GOM and PBM would be rapidly wiped out from the atmosphere after emission due to their significantly greater reactivity, deposition velocities, and water solubility .

Both natural processes and anthropogenic activities release mercury into the atmosphere. Natural sources of mercury include the ocean volatilization, volcanic eruption, evasion from soils and vegetation, geothermal activities, and weathering minerals (Pirrone et al., 2010;Simoneit et al., 2004). Re-emissions of mercury that previously deposited onto the environmental surfaces are also considered as natural source. As for the anthropogenic emission sources of mercury, coal combustion, non-ferrous smelters, cement production, waste incineration, and mining are considered to be the main sources. After being emitted into the atmosphere, mercury undergoes

speciation which plays an important role in its biogeochemical cycle. Previous studies suggest that the oxidation of GEM in the terrestrial environments was generally initiated by O_3 and OH radicals (Mao et al., 2016). Atomic bromine (Br) and bromine monoxide (BrO) are two additional oxidation agents in the marine atmosphere (Xiao et al., 2018;Wang et al., 2016). Observational studies of GOM in the polar regions (Choi et al., 2013;Ye et al., 2016) and in the subtropical marine boundary layer (Cheng et al., 2014;Zhu et al., 2014) as well as atmospheric modeling studies about mercury cycling (Feng et al., 2004;Shon et al., 2005) have considered Br to be an important oxidant of GEM. (Wang et al., 2014) even reported that Br is the primary oxidant of GEM in tropical marine boundary layer (MBL). However, it still remain unknown and controversial about the speciation and quantification of the GEM+O_3 products, and the reaction of GEM+OH is still under huge debate between theoretical and experimental studies due to the lacking of mechanisms consistent with thermochemistry (Xiao et al., 2018). As the GEM converts into GOM, a part of GOM will be adsorbed onto particulate matter since it has high water solubility and relatively strong surface adhesion properties (Liu et al., 2010). GEM accounts for the vast majority of total mercury in the atmosphere, and its concentration is an order of magnitude higher than that of GOM and PBM. Generally, the levels of GEM could be affected by various emission sources, redox reactions, and foliar uptake, while the GOM species from the GEM oxidation and subsequent formation of PBM by adsorption on the particle matters can significantly affect their ambient concentrations, especially in regions with high GEM levels.

Many efforts have been made by governments to reduce mercury emissions. In October 2013, 128 countries signed a global treaty “Minamata Convention on Mercury” in order to reduce mercury emissions from anthropogenic activities (Zhu et al., 2016). However, the mercury pollution issue is still grim especially in Asia, which contribute approximately half of the global mercury emissions (Pacyna et al., 2016). Mainland China plays an important role in the biogeochemical cycling of mercury, since approximately 27% of the global total atmospheric mercury exhausts are from this area (Hui et al., 2017). The Yangtze River Delta (YRD) is one of the most industrialized and urbanized regions in China. Early field measurements in urban Shanghai found that the sources of TGM were most likely derived from coal fired power plants, smelters and industrial activities (Friedli et al., 2011). One study in urban Nanjing indicated that natural sources were important while most sharp peaks of TGM were caused by anthropogenic sources (Zhu et al., 2012). Modeling of

atmospheric mercury in eastern China simulated by the CMAQ-Hg model showed that natural emissions with a contribution of 36.6% were the most important source for GEM in eastern China (Zhu et al., 2015). One study at Chongming (an island belonging to Shanghai) observed a downward trend for GEM concentrations from 2014 to 2016 due to the reduction of domestic emissions (Wang et al., 2016). Studies conducted in Changbai Mountain (Wan et al., 2009) and Xiamen (Xu et al., 2015) used Principal Components Analysis (PCA) to identify potential sources of atmospheric mercury, but the specific contributions of each source couldn't be quantified due to the limitation of the PCA method. Overall, studies with respect to the specific sources and their quantified contributions to atmospheric mercury in the suburbs of East China and the formation and transformation processes among Hg species in the atmosphere are still lacking.

In this study, one-year measurements of GEM, GOM, and PBM were conducted at Dianshan Lake Station (DSL), a suburban site in Shanghai. DSL is located in the junction of Shanghai, Zhejiang, and Jiangsu provinces and is close to the East China Sea (ECS). Few local sources and multiple surroundings make DSL a unique location for studying the main pollution sources and transport pathways of Hg. In this paper, the relationship between Hg and meteorological conditions was revealed; and the oxidation process of GEM to GOM and the adsorption process of GOM on ambient particles were discussed. We also assessed the potential contributing sources of Hg, locating the high potential sources regions and identifying the specific source and their contributions. This study demonstrated the characteristics of atmospheric mercury over an intersection zone and provided insights into the formation of GOM and PBM, and revealed the considerable contribution from shipping activities over the coastal area.

2. Materials and methods

2.1. Site description

The field observation was conducted on the top of a four-story building (~ 14 m) at a super site which is located in the west of Shanghai, and nearby the Dianshan Lake in Qingpu district (Fig. 1). This supersite is carefully maintained by Shanghai Environmental Monitoring Center (SEMC). The building is purely used for atmospheric monitoring without any other usage. DSL lies at suburbs of Shanghai and there are no large point sources around within 20 kilometers, ensuring this site is capable of capturing the meteorological conditions in the study area. Beside the measurement site

is Dianshan Lake, which is the largest freshwater lake in Shanghai with a total area of 62 square kilometers, and next to the site is a highway with moderate traffic. The total GEM emission within a 20 km cycle around the site was around 100kg/yr, indicating weak local human activities. The distance between the sampling site and coastal lines is about 50 km, making it capable of capturing the land-sea circulation. Its special geographical location (at the junction of Shanghai, Zhejiang and Jiangsu provinces) makes it possible to receive the air masses from all these populous regions. In addition, this site is located at the typical outflow path from East China to the Pacific Ocean. The red dots in Fig. 1 represent the amount of atmospheric Hg emitted by anthropogenic activities of each provinces in 2014 (Wu et al., 2016). The emission intensities of anthropogenic Hg in China were higher in the north and lower in the south. The atmospheric Hg emissions by province in 2014 are listed in Table S1.

2.2 Measurement of atmospheric mercury species

Atmospheric mercury species (GEM, GOM, and PBM) were collected and measured from June 2015 to May 2016 using the Tekran 2537B/1130/1135 system (Tekran Inc., Canada). The Tekran system has been widely used and the details have been described elsewhere (Landis and Keeler, 2002). In general, GEM, GOM, and PBM in the atmosphere were collected by dual gold cartridges, KCl-coated annular denuder, and regenerable quartz fiber filter, respectively. In this study, GEM was collected at an interval of 5 minutes with a flow rate of 1 L/min, while GOM and PBM were collected at an interval of 2 hours with a flow rate of 10L/min. After the collection, all mercury species were thermally decomposed to Hg^0 immediately and measured by cold vapor atomic fluorescence spectroscopy (CVAFS). GEM concentrations were expressed in ng/m^3, while GOM and PBM were in pg/m^3 at standard temperature of 273.14K and pressure of 1013 hPa.

A series of work need to be done to ensure the accuracy and validity of the measurement. The KCl-coated denuder, Teflon coated glass inlet, and impactor plate were replaced weekly and quartz filters were replaced monthly. Before sampling, denuders and quartz filters were prepared and cleaned according to the methods in Tekran technical notes. The Tekran 2537B analyzer was routinely calibrated using its internal permeation source every 47 hours, and was also cross-calibrated every 3 months against an external temperature controlled Hg vapor standard. Two-point calibrations (including zero calibration and span calibration) were performed separately for each

pure gold cartridge. Manual injections were performed to evaluate these automated calibrations using the standard saturated mercury vapor.

Quality control on data were also performed during the data analysis. Some extremely high concentrations (especially for GOM and PBM) were occasionally observed. If the values were several times higher than the previous hour, those data were regarded as outliers and were excluded in the data analysis.

2.3 Measurement of other air pollutants and meteorological parameters

Water-soluble inorganic anions (SO_4^{2-}, NO_3^-, Cl^-) and cations (K^+, Mg^{2+}, Ca^{2+}, NH_4^+) in $PM_{2.5}$ were simultaneously monitored by the Monitor for Aerosols and Gases in ambient Air (MARGA) at the resolution of one hour. Ambient air was drawn into a sampling box at a flow rate of 16.7L/min. After removing the water-soluble gases by an absorbing liquid, a supersaturation of water vapor induced the particles in the airflow to grow into droplets, and then the droplets were collected and transported into the analytical box which contains two ion chromatograph systems for the determination of the water-soluble ions in $PM_{2.5}$.

Heavy metals (Pb, Fe, K, Ba, Cr, Se, Cd, Ag, Ca, Mn, Cu, As, Hg, Ni, Zn, V) in $PM_{2.5}$ were measured hourly using the Xact-625 Ambient Metals Monitor (Cooper Environmental services, Beaverton, OR, USA), which is a sampling and analyzing X-ray fluorescence spectrometer designed for online measurements of particulate elements. In this study, ambient air was sampled at a flow rate of 16.7L/min and the particles were collected onto a Teflon filter tape. Then the filter tape was moved into the spectrometer, where it was illuminated with an X-ray tube under three excitation conditions and the excited X-ray fluorescence was measured by a silicon drift detector. Daily advanced quality assurance checks were performed during 30 minutes after midnight to monitor shifts in the calibration.

The hourly meteorological data including air temperature, relative humidity (RH), wind speed, and wind direction were simultaneously monitored at the observation site by the automatic weather station (AWS). The data of the height of planetary boundary layer (PBL) were retrieved from the U.S. National Oceanic and Atmospheric Administration (https://ready.arl.noaa.gov/READYamet.php). Atmospheric ozone (O_3) concentration was continuously measured using Thermo Fisher 49i, which operates on the principle that ozone

molecules absorb UV light at a wavelength of 254 nm. The ambient carbon monoxide (CO) and $PM_{2.5}$ concentrations were measured by Thermo Fisher 48Itle and Thermo Fisher 1405F, respectively. All data were averaged at the intervals of one hour.

2.4 Potential source contribution function (PSCF)

PSCF is a useful tool to diagnose the possible source areas with regard to the levels of air pollutants when setting a contamination concentration threshold at the receptor site. Back trajectory models are used to simulate the airflows. The principle of PSCF is to calculate the ratio of the total number of back trajectory segment endpoints in a grid cell (*i, j*) which exceed the threshold concentration (m_{ij}) to the total number of back trajectory segment endpoints in this grid cell (*i, j*) during the whole sampling period (n_{ij}) as expressed by Equation (1) (Zhang et al., 2017;Cheng et al., 2015).

$$PSCF_{ij} = \frac{m_{ij}}{n_{ij}} \quad (1)$$

When a particular cell is associated with a small number of endpoint, weighting function (w_{ij}) is applied to reduce this uncertainty and the value of w_{ij} is shown in Equation (2) (Fu et al., 2011), in which N_{avg} is the mean n_{ij} of all grid cells with n_{ij} greater than zero. $PSCF_{ij}$ is multiplied by w_{ij} to derive the weighted PSCF values.

$$w_{ij} = \begin{cases} 1.0, & N_{ij} > 3N_{ave} \\ 0.7, & 3N_{ave} > N_{ij} > 1.5N_{ave} \\ 0.4, & 1.5N_{ave} > N_{ij} > N_{ave} \\ 0.2, & N_{ave} > N_{ij} \end{cases} \quad (2)$$

In this study, we set the threshold concentration as the mean value of the whole sampling period. The mean GEM, PBM, and GOM concentrations were 2.77 ng/m^3, 60.8 pg/m^3, and 82.1 pg/m^3, respectively. The HYSPLIT (HYbrid Single-Particle Lagrangian Integrated Trajectory) model is applied for calculating air mass backward trajectories (Draxler and Rolph, 2012). The model was run online at the NOAA ARL READY Website using the meteorological data archives of Air Resource Laboratory (ARL). The meteorological input data used in the model was obtained from NCEP (National Centers for Environmental Prediction)'s global data assimilation system (GDAS) with a horizontal resolution of 0.5° × 0.5°. In this study, 72-hours back trajectories were calculated at 500m AGL (above ground level) and the cell size was set as 0.5°×0.5°.

208

209 **2.5 Positive matrix factorization (PMF)**

210 The PMF model is widely used to quantitatively determine the source contributions of specific
211 air pollutants (Gibson et al., 2015). The essential principle of PMF is that the concentration of each
212 sample is determined by source profiles and different contributions. The equation of the PMF model
213 is shown as Equation (3):

214 $$X_{ij} = \sum_{k=1}^{P} g_{ik} f_{kj} + e_{ij} \quad (3)$$

215 Where X_{ij} is the concentration of the *j*th contamination at the receptor site in the ith sample. g_{ik}
216 represent the contribution of the *k*th factor on the *i*th sample, f_{kj} is used to express the mass fraction
217 of the *j*th contamination in the *k*th factor, *P* is the number of factors, which represent pollution
218 sources, e_{ij} is the residual for each measurement or model error.

219 Before the model determines the optimal non-negative factor contributions and factor profiles,
220 an objective function, which is the sum of the square difference between the measured and modeled
221 concentrations weighted by the concentration uncertainties, has to be minimized (Cheng et al., 2015).
222 The equation that determines the objective function is given by Equation (4):

223 $$Q = \sum_{i=1}^{n} \sum_{j=1}^{m} \left(\frac{X_{ij} - \sum_{k=1}^{p} A_{ik} F_{kj}}{S_{ij}} \right)^2 \quad (4)$$

224 where X_{ij} is the ambient concentration of the *j*th pollutant in the *i*th sample (m and n represent the
225 total number pollutants and samples, respectively). A_{ik} is the contribution of the *k*th factor on the *i*th
226 sample and F_{kj} is the mass fraction of the *j*th pollutant in the *k*th factor. S_{ij} is the uncertainty of the
227 *j*th pollutant on the *i*th measurement, *P* is the number of factors, which imply the pollutant sources.
228 In this study, the number of factors from 3 to 8 was examined with the optimal solutions determined
229 by the slope of the Q value versus the number of factors. For each run, the stability and reliability
230 of the outputs were assessed by referring to the Q value, residual analysis, and correlation
231 coefficients between observed and predicted concentrations. Finally, a 6-factor solution, which
232 showed the most stable results and gave the most reasonable interpretation, was chosen. Before
233 running the model, a dataset including unique uncertainty values of each data point was created and
234 digested into the model. The error fraction was assumed to be 15% of concentrations for GEM and
235 10% of concentrations for the other compounds (Xu et al., 2017), the missing data were excluded
236 and the total number of samples was 3526.

237

3. Results and discussion

3.1. Characteristics of atmospheric mercury species

Fig. 2 displays the time series of atmospheric GEM, PBM, and GOM concentrations during 1 June, 2015 to 31 May, 2016 at DSL. The annual average concentrations of GEM, PBM, and GOM at DSL were 2.77±1.36 ng/m^3, 60.8±67.4 pg/m^3, and 82.1±115.4 pg/m^3, respectively. As shown in Table 1, the levels of GEM and PBM in this study were lower than some sites in China by a factor of 2-7, such as rural Miyun, suburban Xiamen, and urban Guiyang (Xu et al., 2015;Fu et al., 2011). However, compared to the studies conducted in urban and rural areas abroad such as New York (Choi et al., 2013), Chicago (Gratz et al., 2013), and Nova Scotia (Cheng et al., 2014), the concentrations of GEM and PBM in the suburbs of Shanghai were much higher by a factor of 1-3 and 3-8, respectively. Different from GEM and PBM, the GOM concentrations at DSL were higher than all the Chinese sites and other sites around the world listed in Table 1. The mean GOM concentration in this study (82.1 pg/m^3) was even higher than that in Guiyang (35.7 pg/m^3), where the emissions of GEM and GOM were quite intense due to the massive primary emission sources such as coal-fired power plants and cement plants (Fu et al., 2011). The abnormally high GOM concentrations observed in this study were likely dominated by strong primary emissions.

The monthly patterns of GEM, PBM, and GOM during the whole sampling period are shown in Fig. 3. The seasonal mean GEM concentrations were slightly higher in winter (2.88 ng/m^3) and summer (2.87 ng/m^3) than in spring (2.73 ng/m^3) and autumn (2.63 ng/m^3), with the highest monthly mean value of 3.19 ng/m^3 in June and the lowest of 2.39 ng/m^3 in March. Statistical test showed that no significant differences of the seasonal variations of GEM concentrations among spring, summer, and winter were observed (Table S2). This was different from many urban and remote sites in China, such as Guiyang, Xiamen, and Mt. Changbai, where GEM showed significantly high concentrations in cold seasons than those in warm seasons (Feng et al., 2004;Xu et al., 2015;Fu et al., 2012). The relatively high GEM concentrations during the cold season in China should be attributed to the increases of energy consumption (Fu et al., 2015). In this study, GEM concentration in summer was comparable to that in winter, which was likely attributed to the strong natural mercury emissions (e.g. soils, vegetations, and water) due to elevated temperature in summer (Liu et al., 2016). The seasonal mean PBM concentrations were the highest in winter (93.5 pg/m^3) while the lowest in summer (35.7 pg/m^3), and moderate in autumn (56.8 pg/m^3) and spring (51.6 pg/m^3), with the

highest monthly mean value of 109.4 pg/m^3 in January and the lowest of 28.9 pg/m^3 in September. This seasonal pattern was consistent with other sites in China such as Beijing and Nanjing (Zhu et al., 2014;Zhang et al., 2013). PBM concentrations at low altitude sites in the Northern Hemisphere were commonly enhanced in winter, which was ascribed to intense emissions from residential heating, the reduction of wet scavenging processes, enhanced gas-particle partitioning of atmospheric mercury under low temperature, etc. (Rutter and Schauer, 2007). As for GOM, its seasonal mean concentrations were the highest in winter (124.0 pg/m^3), followed by summer (77.3 pg/m^3), spring (68.1 pg/m^3), and autumn (61.0 pg/m^3). GOM concentrations in summer were much lower than that in winter, which were largely due to the more favorable meteorological conditions. However, GOM concentrations in summer were higher than spring and autumn, which should be partly ascribed to the secondary transformation from GEM. More detailed analysis of the impact of meteorological conditions on Hg species and the related formation mechanisms are presented in the following sections.

Fig. 4 shows the diurnal variation of GEM, PBM, and GOM during the whole sampling period. To ensure the time resolutions were consistent among all three mercury species, the temporal resolution of measured GEM was converted from 5 minutes to a two-hour average. As shown in Fig. 4, GEM concentrations were higher during daytime with the maximum in the morning at around 10:00 and minimum in the midnight at around 02:00. The diurnal trends of GOM were as similar as that of GEM, except that the minimum GOM occurred at around 20:00 in the evening. The diurnal trends of PBM were different from those of GEM and GOM, exhibiting relatively higher concentrations during nighttime. The PBM maximum occurred in the early morning at around 6:00 and the minimum was observed in the afternoon at 18:00. The diurnal trends of GEM, PBM, and GOM were as similar as those in Nanjing (Zhu et al, 2012), but different from those in Guiyang, Xiamen, and Guangzhou (Feng et al., 2004;Chen et al., 2013). Since DSL and Nanjing both belongs to the Yangtze River Delta region, the similar meteorology and emission characteristics within the Yangtze River Delta region may explain the similar diurnal patterns of Hg species between DSL and Nanjing. The elevated GEM concentrations at DSL during daytime were likely related to the stronger emissions from both human activities and natural releases. GOM and GEM showed similar diurnal variations and both peaked at 10:00, probably suggesting that GOM and GEM were affected by common sources (e.g. coal-fired power plants and industrial boilers). The high PBM

concentrations at night were likely derived from the adsorption of Hg species onto the preexisting particles and the subsequent accumulation in the shallow nocturnal boundary layer. Fig. 4 shows that wind speed was relatively low while high for relative humidity at night, which were conducive to the adsorption of GOM onto the particles.

3.2. Relationship between Hg species and meteorological factors

Fig. 5 shows the relationship between wind direction/speed and atmospheric mercury species. As shown in Fig. 5a, the prevailing wind at DSL during the study period came from the east, accounting for approximately one-third of all the wind directions. Winds also prevailed from the north with a fraction of 16%. Wind speed from all directions during the study period was mainly in the range of 0-6 m/s, of which wind speed higher than 4 m/s mainly derived from the east. GEM as a function of wind directions showed that the highest GEM concentrations were linked to the winds from the south and southwest with the mean value of 3.92 ng/m^3, while the mean GEM concentration from the other wind sectors was 2.71 ng/m^3 (Fig. 5b). GOM showed similar wind-concentration patterns as GEM. While PBM showed high concentrations from the north/northwest and south/southwest (Fig. 5c &5d). By referring to Fig. 1, the anthropogenic mercury emissions in northern China were generally higher than southern China. Hence, the observation of high atmospheric Hg concentrations from the north was expected. In this regard, the even higher atmospheric Hg concentrations from the south and southeast than from the north cannot be simply explained by anthropogenic emission sources, implying that there must be additional Hg emission sources. (Feng et al., 2004) reported that the Hg concentrations in the surface soils of southern China were generally higher than the northern China. A modeling study simulated that the mean annual Hg air-soil flux in the southwest region of our sampling site (e.g. Zhejiang province) ranged from 8.75 to 15 ng m^{-2} h^{-1}, while that in the north/northwest region (e.g. Jiangsu province) ranged from 2.5 to 8.75 ng m^{-2} h^{-1} (Wang et al., 2016). Hence, emissions from natural sources, such as soils, vegetations and water, should play an important role in the observed high atmospheric Hg concentrations from the south and southeast.

In order to confirm this conjecture, the relationship between temperature and Hg concentrations at DSL was investigated. Seasonal temperature in ascending order was divided into different groups and the corresponding mean Hg concentrations were plotted in Fig. 6. In spring, the GEM

concentrations increased as the temperature increased. As for the other season, when the temperature increased to a certain value, the trends of GEM variations were as similar as spring. This relationship between GEM and temperature can be likely interpreted as the impact of surface emissions. It must be noted that the height of PBL increased as the temperature increased, while at the same time, GEM still showed a significant upward trend. This suggested that the atmospheric dilution effect caused by the developing boundary layer was far from offsetting the increase of surface emissions caused by increased temperature. The GOM concentration showed a clearly positive correlation with temperature in summer. Higher temperature in summer in the Yangtze River Delta region is mostly associated with ozone pollution days (Lu et al., 2018), thus implying higher GOM could be partially related to the in situ oxidation of GEM in addition to its sources from direct emissions. In the other seasons, no clear correlations between GOM and temperature were observed. As for PBM, it appeared to have weakly negative correlations with the height of PBL, suggesting the atmospheric diffusion conditions were influential on the concentrations of PBM.

3.3. Tracing sources of Hg species

3.3.1. Potential source regions of Hg species

PSCF was applied to identify the potential source regions of the three Hg species. As for GEM, the major source areas were located in Anhui, Jiangxi, and Zhejiang provinces, and there were also signals from Shandong province (Fig. 7a). As for the seasonal pattern (Fig. S1), the potential source regions of GEM in spring were mainly from Jiangsu and Zhejiang provinces. In summer, the PSCF hotspots were identified in Anhui and Jiangxi provinces. Jiangsu province was likely to become the main potential source region of GEM in autumn. In winter, Anhui and Zhejiang provinces showed relatively high PSCF values. In addition, there were also signals from Henan and Shandong provinces, suggesting the importance of long-range transport in wintertime. There existed substantial high PSCF signals in the southern areas, even stronger than those in the north. However, as shown in Fig. 1, southern provinces such as Zhejiang and Jiangxi were estimated to release 25 tons/yr atmospheric Hg from anthropogenic activities, being far less than the northern provinces such as Jiangsu and Shandong (77 tons/yr) (Wu et al., 2016). If only the anthropogenic emissions of GEM were considered, the occurrence of stronger PSCF signals in southern provinces seemed unreasonable. Based on the mean annual Hg air-soil flux of 8.75 to 15 ng m^{-2} h^{-1} in the southwest

region of our sampling site (Wang et al., 2016), it was estimated that the total Hg emissions from soils were in the range of 6.9 - 13.9 tons/yr for Zhejiang province. As for the anthropogenic Hg emission of Zhejiang province in 2014, it was approximately 15tons/yr (Wu et al., 2016). Thus, the magnitude of mercury from natural surfaces was comparable to that from anthropogenic sources. In this regard, the re-emission of GEM from natural surfaces in southern areas should be an important source, corroborating the discussion in Section 3.2. In addition, the East China Sea (including the offshore areas and open ocean) showed sporadic high PSCF signals of GEM in all four seasons (Fig. S1), indicating possible influences from shipping activities. The detailed estimation of variable sources would be discussed in Section 3.3.3.

The PSCF pattern of PBM was quite different from that of GEM (Fig. 7b). The potential source regions of all year round PBM were mainly from the north of Jiangsu and Anhui provinces, and from northeastern China, including Shandong and Hebei provinces. These provinces were regarded as the main Hg sources areas in China and accounted for approximately 25.2% of the Chinese anthropogenic atmospheric Hg emissions (Wu et al., 2016). As for the seasonal PSCF patterns of PBM (Fig. S2), its potential source regions in spring, autumn, and winter shared certain commonalities that exhibited the consistent PSCF patterns as the annual pattern. The exception was found for summer, which showed high PSCF values mainly in the southern areas of Shanghai. This might be attributed to that the prevailing winds in summer were from the south, southeast, and southwest where Zhejiang and Jiangxi provinces were important mercury source regions.

The potential source regions of all year round GOM were mainly located in Anhui and Zhejiang provinces and the coastal areas along Jiangsu province (Fig. 7c). The PSCF pattern of GOM was as similar as that of GEM but different from that of PBM. The potential source regions of GOM were more from southern China rather than from northern China, which might be due to the higher atmospheric oxidant levels in the southern regions. Especially in summer, the potential sources regions of GOM concentrated in Zhejiang and Jiangxi provinces (Fig. S3). In the other seasons, there were somewhat different PSCF patterns observed. In detail, while significant PSCF signals from the inland areas were found, moderate PSCF signals over the East China Sea and Yellow Sea also observed in spring. In autumn, the high PSCF values mainly occurred in Zhejiang province and there were also moderate signals over the Yellow Sea. In winter, the high PSCF values spread from the coastal areas of Jiangsu to a vast ocean of the Yellow Sea. One previous study suggested that the

388 marine boundary layer could provide considerable amounts of oxidants such as chlorine and
389 bromine, which were beneficial for the production of GOM by oxidizing GEM (Auzmendi-Murua
390 et al., 2014) and this may explain the substantial PSCF signals over the ocean.
391 The results of the PSCF analysis suggested the significant influences of adjacent areas of
392 Shanghai on contributing to all the atmospheric mercury species. It was also illustrated that the long-
393 range and regional transport via both land transport and sea breeze were important.
394
395 **3.3.2. Comparison between the impact of quasi-local sources and regional/long-range**
396 **transport on atmospheric mercury**
397 According to the relationship between wind direction and Hg species as well as the PSCF
398 analysis discussed above, the elevated GEM, GOM, and PBM concentrations at the observation site
399 were generally related to the wind sectors from the southwest and north. In order to reveal the
400 relative importance of local sources and regional transport, the ratio of GOM/PBM was applied as
401 an indicator based on the fact that the residence time of GOM is generally considered to be shorter
402 than that of PBM. If regional/long-range transport was evident, the ratio of GOM/PBM should be
403 lower due to that GOM was more quickly scavenged than PBM during the transport, and vice versa
404 when local sources dominated. In this regard, the ratios of GOM/PBM during the whole study period
405 were grouped into four categories, i.e. 0-1, 1-2, 2-3, and higher than 3. The corresponding frequency
406 of wind direction in each category was compared in Fig. 8. It was clear that the higher GOM/PBM
407 ratios were associated with more frequent winds from the east and southeast. The frequency of these
408 two wind sectors increased significantly from 27% under the GOM/PBM ratios less than 1 to 52%
409 under the GOM/PBM ratios higher than 3. Winds from the east and southeast were typically
410 characterized of relatively clean air masses, suggesting the local sources around the observational
411 site should dominate. In contrast, the lower GOM/PBM ratios were associated with more frequent
412 winds clockwise from the west to the north and the frequency of these wind sectors decreased
413 significantly from 44% under the GOM/PBM ratios less than 1 to 21% under the GOM/PBM ratios
414 higher than 3. These winds were indicative of the long-range/regional transport from northern China
415 and were associated with the relatively low GOM/PBM ratios. According to the PSCF results above,
416 the potential source areas of Hg species (GEM, GOM and PBM) derived mostly from the south and
417 southwest of the sampling site. As shown in Fig. 8, the frequency of south, southwest, west, and

northeast winds showed no clear trend as the GOM/PBM ratios increased. This suggested the emissions of Hg in these directions of the sampling site were complicated, and the phenomenon above can not be simply explained by the impact of local sources or regional transport. In general, the GOM/PBM ratio can be used as a qualitative tracer for identifying the relative importance of long-range transport vs. local sources. However, when the influences from long-range transport and local emission were close, the result could be ambiguous based on this method and this may require further efforts such as chemical transport modeling.

The relationships among GEM, CO, secondary inorganic aerosols (SNA) and GOM/PBM ratios were further investigated. Fig. 9 displays the concentrations of GEM as a function of GOM/PBM ratios colored by CO. The sizes of the circles represented the corresponding concentrations of SNA in $PM_{2.5}$. CO was commonly used as a tracer of fuel combustion and SNA were derived from secondary particle formation via the gas-to-particle conversion. CO and SNA were collectively used as proxies of the extent of anthropogenic air pollutants and especially for evaluating the extent of regional/long-range transport. As shown in Fig. 9, GEM showed an overall increasing trend as the GOM/PBM ratios increased. In addition, it could be clearly seen that the lower GOM/PBM ratios were associated with higher CO and SNA concentrations and vice versa. This corroborated the discussion above that the GOM/PBM ratio was a reliable tracer for assessing the relative importance of regional/long-range transport vs. local atmospheric processing.

In the GOM/PBM ratio bins of less than 2.5, GEM fluctuated with the mean values less than 2.6 ng/m^3. The mean GEM concentration increased from 2.61 ng/m^3 in the GOM/PBM ratio bin of 2.5-3.0 to 2.8 ng/m^3 in the bin of 3.0-3.5, and then remain relatively stable when the GOM/PBM ratio bins higher than 3.0. Generally, GEM showed an increasing trend as the GOM/PBM ratios increased while both SNA and CO decreased. The elevation of GEM concentrations tended to be associated with the impact of quasi-local sources. In contrast, under the high SNA and CO conditions when GOM/PBM ratios were lower, GEM showed relatively low concentrations. This suggested the regional/long-range transport didn't favor the elevation of GEM concentrations. It has been recognized that the common regional/long-range transport pathways on contributing to the particulate pollution events of Shanghai were from the north and northwest originating mostly from the North China Plain. The relatively lower GEM concentrations under the regional/long-range transport conditions corroborated the PSCF analysis that only moderate probabilities of GEM source

regions from northern China were found (Fig. 7a).

3.3.3. Source apportionment by combined PMF and PCA

PMF modeling has been widely used to apportion the sources of atmospheric pollutants. In this study, GEM together with heavy metals and soluble ions, measured online synchronously, were introduced into the EPA PMF5.0 model to apportion the major anthropogenic sources of GEM. A six-factor solution was selected based on the results of multiple model runs, which can well explain the measured concentrations of the introduced species. The profiles of six identified PMF factors and contributions of major anthropogenic sources to GEM are shown in Fig. 10. It has to be noted that since no tracers for the natural emissions (e.g. soils, vegetations, and ocean) were available in this study, the identification of natural mercury sources was not possible based on the PMF modeling.

Factor 1 had high loadings for Se, As, Pb, NO_3^-, SO_4^{2-}, and NH_4^+. Se, As, and Pb were typical tracers of coal combustion. SO_4^{2-} and NO_3^- were also formed from the gaseous pollutants emitted from coal burning. Hence, this factor was defined as coal combustion sources and accounted for 12.3% of the anthropogenic GEM. Fig. S4 plotted wind roses of specific aerosol species. Of which, SO_4^{2-} and As shared similar patterns with high concentrations mainly from the southwest. Since combustion was an important source of GEM, this confirmed that the major sources of GEM were located in the southwest region.

Factor 2 displayed particularly high loadings for Ni and V. The major sources of Ni in the atmosphere can be derived from coal and oil combustions (Tian et al., 2012), and oil combustion accounted for 85% of anthropogenic V emissions in the atmosphere (Duan and Tan, 2013). In general, Ni and V have been considered as good tracers of heavy oil combustion, which has been commonly used in marine vessels (Viana et al., 2009). Thus, this factor was identified as shipping emissions. The sampling site is adjacent to the East China Sea and is located in Shanghai which has the largest port in the world. Fig. S4 showed similar patterns of Ni and V with high concentrations mainly from the northeast, east, and southeast. To further validate this factor, the time-series of GEM concentrations from the shipping factor based on the PMF modeling were extracted and digested into the PSCF modeling (Fig. S5), showed that the potential sources regions were mainly located over the East China Sea and coastal regions. This indicated factor 2 from PMF should be representative of the shipping sector as well as oil combustion in motor vehicles and inland shipping

activities. Overall, this factor accounted for 19.6% of anthropogenic GEM and ranked as the second largest emission sector, highlighting the urgent need of controlling the marine vessel emissions.

Factor 3 showed high loadings for Ca and moderate loadings for Ba and Fe. Ca and Fe are rich elements in crust that can be used for cement production. As mercury could be released during industrial processes of cement production, Factor 3 was assigned as cement production and accounted for a minor fraction of 6.3 % of the anthropogenic GEM.

Factor 4 was characterized by high loadings of Cr and moderate loadings of Mn, Fe, Ni, and Cu. These species together served as markers of metals smelting. Metals smelting were known to be large sources of Hg emitted to the atmosphere (Pirrone et al., 2010), especially in the YRD, one of the most developed and industrialized areas in China. This factor accounted for 7.6% of the anthropogenic GEM.

Factor 5 had high loadings of Cl^-. Waste incineration is an important source of enriched chloride over land. Factor 5 was identified to be waste incineration, which contributed 6.4% of the anthropogenic GEM.

Factor 6 was characterized by high loadings of Cd, Ag, K^+, and Na^+. The major sources of Cd in China were iron and steel smelting industries (Duan and Tan, 2013). Ag was mainly used in industrial applications, including electronic appliances and photographic materials. K^+ was a typical tracer of biomass burning, which often stemmed from agriculture waste burning over the Yangtze River Delta and the North China Plain. In this regard, Factor 6 was considered as a combined source of the industrial and biomass burning emission sectors. It was estimated to contribute 47.8% of the anthropogenic GEM.

As discussed in the above sections, surface emissions were likely to be important sources of the observed atmospheric mercury. As PMF modeling didn't resolve the natural sources of mercury, the PCA (Principal Component Analysis) was applied for further source apportionment by introducing the temperature parameter. Four factors are resolved, which totally explained 75.32% of the variance as shown in Table 2. Factor 1 accounted for 34.15% of the total variance with high loadings for SO_2, SO_4^{2-}, NH_4^+, K^+, Pb, Se, and As, which was explained as coal combustion mixed with biomass burning. Factor 2 accounted for 14.85% of the total variance with high loadings for temperature, O_3, and NH_3, which was explained as surface emissions. Factor 3 explained 13.43% of the total variance and showed high loadings for Ni and V, which indicated the contribution of

ship emissions. Factor 4 explained 12.89% of the total variance and showed high loading for Fe and Ca, indicating the contribution of cement production.

3.4. Factors affecting the formation and transformation of mercury species

3.4.1. Factors affecting the formation of GOM

A typical case from July 24 to July 27, 2015 was chosen to investigate the possible formation process of GOM. As shown in Fig. 11, the shaded episodes represented nighttime from 18:00 to 6:00 the next day. Both GEM and GOM exhibited rising trends during nighttime (Fig. 11a), which was ascribed to nighttime accumulation effect due to the very shallow boundary layer (Fig. 11c). Starting from 6:00 in the morning, GEM concentrations began to gradually decline as the boundary layer developed. In contrast, the concentrations of GOM continued to rise from 6:00 until it reached the peak value at around 10:00. During this period, the levels of ozone and temperature also kept rising until surpassed 200 μg/m^3 and 34°C, respectively. Accordingly, as an anthropogenic emitting tracer, the concentration of carbon monoxide was basically stable and even showing a downward trend, which suggested some other factors accounted for the increase of GOM in addition to the anthropogenic emissions. This phenomenon clearly revealed the acceleration of the conversion process of GEM to GOM under favorable atmospheric conditions of higher O_3 concentration and ambient temperature. In the case of atmosphere dilution by the rise of PBL, the fact that GOM was not falling but rising suggested the great influence of this process on ambient GOM concentrations. Similar observation has been found at the high-altitude Pic du Midi observatory in southern France (Fu et al., 2016), which was almost impervious to anthropogenic emission sources. The important role of GEM oxidation in our sampling site, which located in one of the most developed industrial areas in China, was most likely due to the presence of sufficient oxidants in this area. Severe ozone pollution frequently occurred in the YRD due to strong anthropogenic emission intensities (Lu et al., 2018). Previous studies suggested that the primary oxidants in the terrestrial environment were O_3 and OH radicals (Shon et al., 2005), while Br was an important oxidant in the subtropical marine boundary layer (Obrist et al., 2011). It was possible that, in addition to O_3 and OH radicals, Br might also be an important inducing species to the oxidation of GEM as the DSL site is adjacent to the East China Sea.

Fig. 12 statistically analyzed the relationship among GOM, O_3, and temperature. Temperature was plotted against a range of GOM/PBM bins colored by O_3 and the size of the circles represented the concentrations of GOM. In general, as temperature and O_3 increased, the concentrations of GOM were subject to substantial enhancement. For instance, when temperature (O_3) was below 12℃ (65.7 μg/m^3), GOM averaged 37.8 pg/m^3. While temperature (O_3) increased to above 20℃ (91.5 μg/m^3), GOM rose to 168.8 pg/m^3, yielding a factor of 1- 5 GOM increases. This further confirmed the case study above that the levels of oxidants under favorable environmental conditions were crucial for the formation of GOM. Fig. 12 also suggested that the lower ratios of GOM/PBM were associated with lower temperature and O_3 concentrations, indicating relatively weak photochemistry during the cold seasons. On the contrary, the higher ratios of GOM/PBM were associated with higher temperature and O_3 concentrations, indicating relatively strong photochemistry during the warm seasons. This suggested that the formation of GOM was more favored by local atmospheric processing rather than the transport. This study demonstrated the abnormally high GOM concentrations observed at DSL were largely ascribed to local oxidation reactions. However, the explicit formation mechanism of GOM need to be investigated by measuring more detailed components of GOM and atmospheric oxidants.

3.4.2. Factors affecting the transformation of PBM

Previous studies have shown that PBM can be emitted directly from various anthropogenic sources such as coal-fired power plants and industries (Liu et al., 2018;Wu et al., 2016). In addition, gas-particle partitioning was considered to be an important pathway for the formation of PBM (Shon et al., 2005;Amos et al., 2012). Since most of the areas in the YRD belong to non-attainment areas in regard of particulate pollution and the concentrations of GOM were particularly high at DSL as discussed above, the role of gas-particle partitioning in the formation of PBM should be investigated. Previous studies reported that the concentrations of $PM_{2.5}$ in eastern and northern China are highest in the world (Auzmendi-Murua et al., 2014), elevated atmospheric particulate matter probably facilitates the formation of PBM in the atmosphere in China (Fu et al., 2015). Fig. 13 shows the statistical pattern of the variation of PBM and GOM in the ascending bins of $PM_{2.5}$. The concentrations of PBM increased with the concentrations of $PM_{2.5}$, which was due to both primary emissions and the subsequent process of Hg species adsorbed on particulate matters. The

trend of GOM was somehow different from that of PBM. When $PM_{2.5}$ concentrations were at relatively low levels under 75 μg/m^3, GOM concentrations increased with $PM_{2.5}$. However, when $PM_{2.5}$ concentrations increased to 75-105 μg/m^3, GOM exhibited a clear decreasing trend as $PM_{2.5}$ increased. It seemed that when the concentration of $PM_{2.5}$ reached a certain value, the formation of GOM was inhibited to some extent, which was likely due to the adsorption of GOM onto the particles. When $PM_{2.5}$ concentrations exceeded 105 μg/m^3, GOM exhibited a slightly increasing trend as $PM_{2.5}$ increased. High $PM_{2.5}$ concentrations in China always related to severe anthropogenic emissions (Auzmendi-Murua et al., 2014), so the moderate increasing trend of GOM in these bins should be attributed to the impact of strong primary emissions.

A short episode from December 30, 2015 to January 1, 2016 was chosen to further investigate this phenomenon. As shown in Fig. 14, in Stage 1, the concentrations of $PM_{2.5}$ were below 100 μg/m^3, PBM and GOM shared the similar temporal variation as $PM_{2.5}$. In Stage 2, as $PM_{2.5}$ kept climbing, GOM began to show somewhat negative correlation with $PM_{2.5}$, but not significant. The reason might be that the relatively high temperature and low humidity during this period were not conducive to the transfer of GOM to particle matters. In Stage 3, GOM decreased as $PM_{2.5}$ continued to increase, showing a clear anti-correlation. During this period, PBM showed a consistent trend with $PM_{2.5}$ and CO. Temperature was relatively low but with relatively high humidity. This phenomenon clearly demonstrated the process of gas-particle partitioning of PBM formation. In stage 4, GOM and PBM showed similar decreasing trend with $PM_{2.5}$ and CO. The low GOM concentrations, low humidity, and high temperature resulted in no significant signs of GOM adsorption to $PM_{2.5}$ in this stage. In general, under high $PM_{2.5}$ and GOM concentrations, high humidity and low temperature conditions in our sampling site, clear processes of gas-particle partitioning were observed .

4. Conclusions

In this study, a year-long observation of three atmospheric Hg species was conducted at the Dianshan Lake (DSL) Observatory, located on the typical transport routes from mainland China to the East China Sea. During the whole measurement period, the mean GEM, PBM, and GOM concentrations were 2.77 ng/m^3, 60.8 pg/m^3, and 82.1 pg/m^3, respectively.

Different from many sites in China, GEM at DSL exhibited high concentrations in winter,

summer, and spring, which was due to the strong re-emission fluxes from natural surfaces in summer and enhanced coal combustion for residential heating over northern China in winter. The relatively high GOM concentrations in summer indicated that the formation of GOM from GEM oxidation was likely crucial. PBM exhibited high concentrations in winter, indicating the impact from long-range transport. The diurnal patterns of GEM and GOM were similar with relatively high levels during daytime. For GEM, this was likely attributed to both human activities and re-emission from natural surfaces during daytime. For GOM, in addition to direct emissions, high concentrations during daytime were partially ascribed to photochemical oxidation of GEM. The PBM concentrations were higher during nighttime, which was ascribed to the accumulation effect within the shallow nocturnal boundary layer.

The relationship between meteorological factors and atmospheric Hg species showed that the high Hg concentrations were generally related to the winds from the south, southwest, and north and positively correlated with temperature. Both anthropogenic sources and natural sources contributed to the atmospheric mercury pollution at DSL. Higher GOM/PBM ratios corresponded to lower CO and SNA concentrations and vice versa. The ratio of GOM/PBM can be used as a tracer for distinguishing local sources and regional/long-range transport based on the fact that the residence time of GOM was shorter than that of PBM. GEM as a function of the GOM/PBM ratios indicated that when the quasi-local sources dominated, GEM concentrations were relatively higher than those events under the regional/long-range transport conditions. According to the PMF source apportionment results, six sources of anthropogenic GEM and their contributions were identified, i.e. industrial and biomass burning (47.8%), shipping emission (19.6%), coal combustion (12.3%), iron and steel production (7.6%), incineration (6.4%), and cement production (6.3%). The significant contribution of shipping emission suggested that in coastal areas mercury emitted from marine vessels can be significant. In addition, a considerable natural source of GEM was identified by digesting temperature into the principle component analysis.

The formation processes of GOM and PBM based on episodic studies were also investigated. The high GOM concentrations were partially attributed to strong local photochemical reactions under the conditions of high O_3 and temperature. Under high $PM_{2.5}$ concentrations, high humidity and low temperature conditions, the gas-particle partitioning processes were observed at DSL, which might be an important pathway for the formation of PBM.

Author contributions. KH, CD, and XQ conceived the study and wrote the paper. XW, YL, and DW performed the measurements and collected data. All have contributed to the data analysis and review of the manuscript.

Acknowledgements

This work was supported by the Natural Science Foundation of China (NSFC, Grant Nos. 91644105, 21777029), the National Key R&D Program of China (Grant Nos. 2018YFC0213105), and Environmental Charity Project of Ministry of Environmental Protection of China (201409022).

References

Amos, H. M., Jacob, D. J., Holmes, C. D., Fisher, J. A., Wang, Q., Yantosca, R. M., Corbitt, E. S., Galarneau, E., Rutter, A. P., Gustin, M. S., Steffen, A., Schauer, J. J., Graydon, J. A., Louis, V. L. S., Talbot, R. W., Edgerton, E. S., Zhang, Y., and Sunderland, E. M.: Gas-particle partitioning of atmospheric Hg(II) and its effect on global mercury deposition, Atmos. Chem. Phys., 12, 591-603, 10.5194/acp-12-591-2012, 2012.

Auzmendi-Murua, I., Castillo, A., and Bozzelli, J. W.: Mercury Oxidation via Chlorine, Bromine, and Iodine under Atmospheric Conditions: Thermochemistry and Kinetics, Journal of Physical Chemistry A, 118, 2959-2975, 10.1021/jp412654s, 2014.

Chen, L. G., Liu, M., Xu, Z. C., Fan, R. F., Tao, J., Chen, D. H., Zhang, D. Q., Xie, D. H., and Sun, J. R.: Variation trends and influencing factors of total gaseous mercury in the Pearl River Delta-A highly industrialised region in South China influenced by seasonal monsoons, Atmospheric Environment, 77, 757-766, 10.1016/j.atmosenv.2013.05.053, 2013.

Cheng, I., Zhang, L. M., Mao, H. T., Blanchard, P., Tordon, R., and Dalziel, J.: Seasonal and diurnal patterns of speciated atmospheric mercury at a coastal-rural and a coastal-urban site, Atmospheric Environment, 82, 193-205, 10.1016/j.atmosenv.2013.10.016, 2014.

Cheng, I., Xu, X., and Zhang, L.: Overview of receptor-based source apportionment studies for speciated atmospheric mercury, Atmos. Chem. Phys., 15, 7877-7895, 10.5194/acp-15-7877-2015, 2015.

Choi, H. D., Huang, J. Y., Mondal, S., and Holsen, T. M.: Variation in concentrations of three mercury (Hg) forms at a rural and a suburban site in New York State, Sci. Total Environ., 448, 96-106, 10.1016/j.scitotenv.2012.08.052, 2013.

Draxler, R., and Rolph, G.: HYSPLIT - Hybrid Single Particle Lagrangian Integrated Trajectory Model, 2012.

Duan, J., and Tan, J.: Atmospheric heavy metals and Arsenic in China: Situation, sources and control policies, Atmospheric Environment, 74, 93-101, 10.1016/j.atmosenv.2013.03.031, 2013.

Feng, X. B., Shang, L. H., Wang, S. F., Tang, S. L., and Zheng, W.: Temporal variation of total gaseous mercury in the air of Guiyang, China, J. Geophys. Res.-Atmos., 109, 10.1029/2003jd004159, 2004.

Friedli, H. R., Arellano, A. F., Geng, F., Cai, C., and Pan, L.: Measurements of atmospheric mercury in Shanghai during September 2009, Atmospheric Chemistry and Physics, 11, 3781-3788, 10.5194/acp-11-3781-2011, 2011.

Fu, X., Marusczak, N., Heimbürger, L.-E., Sauvage, B., Gheusi, F., Prestbo, E. M., and Sonke, J. E.:

667 Atmospheric mercury speciation dynamics at the high-altitude Pic du Midi Observatory, southern
668 France, Atmospheric Chemistry and Physics, 16, 5623-5639, 10.5194/acp-16-5623-2016, 2016.
669 Fu, X. W., Feng, X. B., Qiu, G. L., Shang, L. H., and Zhang, H.: Speciated atmospheric mercury and its
670 potential source in Guiyang, China, Atmospheric Environment, 45, 4205-4212,
671 10.1016/j.atmosenv.2011.05.012, 2011.
672 Fu, X. W., Feng, X., Shang, L. H., Wang, S. F., and Zhang, H.: Two years of measurements of atmospheric
673 total gaseous mercury (TGM) at a remote site in Mt. Changbai area, Northeastern China, Atmospheric
674 Chemistry and Physics, 12, 4215-4226, 10.5194/acp-12-4215-2012, 2012.
675 Fu, X. W., Zhang, H., Yu, B., Wang, X., Lin, C. J., and Feng, X. B.: Observations of atmospheric mercury in
676 China: a critical review, Atmospheric Chemistry and Physics, 15, 9455-9476, 10.5194/acp-15-9455-2015,
677 2015.
678 Gibson, M. D., Haelssig, J., Pierce, J. R., Parrington, M., Franklin, J. E., Hopper, J. T., Li, Z., and Ward, T. J.:
679 A comparison of four receptor models used to quantify the boreal wildfire smoke contribution to surface
680 PM2.5 in Halifax, Nova Scotia during the BORTAS-B experiment, Atmospheric Chemistry and Physics, 15,
681 815-827, 10.5194/acp-15-815-2015, 2015.
682 Gratz, L. E., Keeler, G. J., Marsik, F. J., Barres, J. A., and Dvonch, J. T.: Atmospheric transport of speciated
683 mercury across southern Lake Michigan: Influence from emission sources in the Chicago/Gary urban
684 area, The Science of the total environment, 448, 84-95, 10.1016/j.scitotenv.2012.08.076, 2013.
685 Hui, M. L., Wu, Q. R., Wang, S. X., Liang, S., Zhang, L., Wang, F. Y., Lenzen, M., Wang, Y. F., Xu, L. X., Lin,
686 Z. T., Yang, H., Lin, Y., Larssen, T., Xu, M., and Hao, J. M.: Mercury Flows in China and Global Drivers,
687 Environmental science & technology, 51, 222-231, 10.1021/acs.est.6b04094, 2017.
688 Landis, M. S., and Keeler, G. J.: Atmospheric mercury deposition to Lake Michigan during the Lake
689 Michigan Mass Balance Study, Environmental science & technology, 36, 4518-4524, 10.1021/es011217b,
690 2002.
691 Liu, B., Keeler, G. J., Dvonch, J. T., Barres, J. A., Lynam, M. M., Marsik, F. J., and Morgan, J. T.: Urban-rural
692 differences in atmospheric mercury speciation, Atmospheric Environment, 44, 2013-2023,
693 10.1016/j.atmosenv.2010.02.012, 2010.
694 Liu, K., Wang, S., Wu, Q., Wang, L., Ma, Q., Zhang, L., Li, G., Tian, H., Duan, L., and Hao, J.: A Highly
695 Resolved Mercury Emission Inventory of Chinese Coal-Fired Power Plants, Environmental science &
696 technology, 52, 2400-2408, 10.1021/acs.est.7b06209, 2018.
697 Liu, M. D., Chen, L., Wang, X. J., Zhang, W., Tong, Y. D., Ou, L. B., Xie, H., Shen, H. Z., Ye, X. J., Deng, C. Y.,
698 and Wang, H. H.: Mercury Export from Mainland China to Adjacent Seas and Its Influence on the Marine
699 Mercury Balance, Environmental science & technology, 50, 6224-6232, 10.1021/acs.est.5b04999, 2016.
700 Lu, X., Hong, J., Zhang, L., Cooper, O. R., Schultz, M. G., Xu, X., Wang, T., Gao, M., Zhao, Y., and Zhang, Y.:
701 Severe Surface Ozone Pollution in China: A Global Perspective, Environmental Science & Technology
702 Letters, 10.1021/acs.estlett.8b00366, 2018.
703 Mao, H. T., Cheng, I., and Zhang, L. M.: Current understanding of the driving mechanisms for
704 spatiotemporal variations of atmospheric speciated mercury: a review, Atmospheric Chemistry and
705 Physics, 16, 12897-12924, 10.5194/acp-16-12897-2016, 2016.
706 Marsik, F. J., Keeler, G. J., and Landis, M. S.: The dry-deposition of speciated mercury to the Florida
707 Everglades: Measurements and modeling, Atmospheric Environment, 41, 136-149,
708 10.1016/j.atmosenv.2006.07.032, 2007.
709 Obrist, D., Tas, E., Peleg, M., Matveev, V., Fain, X., Asaf, D., and Luria, M.: Bromine-induced oxidation of
710 mercury in the mid-latitude atmosphere, Nat. Geosci., 4, 22-26, 10.1038/ngeo1018, 2011.

Pacyna, J. M., Travnikov, O., De Simone, F., Hedgecock, I. M., Sundseth, K., Pacyna, E. G., Steenhuisen, F., Pirrone, N., Munthe, J., and Kindbom, K.: Current and future levels of mercury atmospheric pollution on a global scale, Atmos. Chem. Phys., 16, 12495-12511, 10.5194/acp-16-12495-2016, 2016.

Pirrone, N., Cinnirella, S., Feng, X., Finkelman, R. B., Friedli, H. R., Leaner, J., Mason, R., Mukherjee, A. B., Stracher, G. B., Streets, D. G., and Telmer, K.: Global mercury emissions to the atmosphere from anthropogenic and natural sources, Atmos. Chem. Phys., 10, 5951-5964, 10.5194/acp-10-5951-2010, 2010.

Rutter, A. P., and Schauer, J. J.: The effect of temperature on the gas-particle partitioning of reactive mercury in atmospheric aerosols, Atmospheric Environment, 41, 8647-8657, 10.1016/j.atmosenv.2007.07.024, 2007.

Shon, Z. H., Kim, K. H., Kim, M. Y., and Lee, M.: Modeling study of reactive gaseous mercury in the urban air, Atmospheric Environment, 39, 749-761, 10.1016/j.atmosenv.2004.09.071, 2005.

Simoneit, B. R. T., Elias, V. O., Kobayashi, M., Kawamura, K., Rushdi, A. I., Medeiros, P. M., Rogge, W. F., and Didyk, B. M.: Sugars - Dominant water-soluble organic compounds in soils and characterization as tracers in atmospheric particulate matter, Environmental science & technology, 38, 5939-5949, 10.1021/es0403099, 2004.

Tian, H. Z., Lu, L., Cheng, K., Hao, J. M., Zhao, D., Wang, Y., Jia, W. X., and Qiu, P. P.: Anthropogenic atmospheric nickel emissions and its distribution characteristics in China, Sci. Total Environ., 417, 148-157, 10.1016/j.scitotenv.2011.11.069, 2012.

Viana, M., Amato, F., Alastuey, A., Querol, X., Moreno, T., Garcia Dos Santos, S., Dolores Herce, M., and Fernandez-Patier, R.: Chemical Tracers of Particulate Emissions from Commercial Shipping, Environmental science & technology, 43, 7472-7477, 10.1021/es901558t, 2009.

Wan, Q., Feng, X. B., Lu, J. L., Zheng, W., Song, X. J., Han, S. J., and Xu, H.: Atmospheric mercury in Changbai Mountain area, northeastern China I. The seasonal distribution pattern of total gaseous mercury and its potential sources, Environmental Research, 109, 201-206, 10.1016/j.envres.2008.12.001, 2009.

Wang, F., Saiz-Lopez, A., Mahajan, A. S., Martin, J. C. G., Armstrong, D., Lemes, M., Hay, T., and Prados-Roman, C.: Enhanced production of oxidised mercury over the tropical Pacific Ocean: a key missing oxidation pathway, Atmospheric Chemistry and Physics, 14, 1323-1335, 10.5194/acp-14-1323-2014, 2014.

Wang, X., Lin, C.-J., Yuan, W., Sommar, J., Zhu, W., and Feng, X.: Emission-dominated gas exchange of elemental mercury vapor over natural
surfaces in China, Atmospheric Chemistry and Physics, 16, 11125-11143, 10.5194/acp-16-11125-2016, 2016.

Wu, Q. R., Wang, S. X., Li, G. L., Liang, S., Lin, C. J., Wang, Y. F., Cai, S. Y., Liu, K. Y., and Hao, J. M.: Temporal Trend and Spatial Distribution of Speciated Atmospheric Mercury Emissions in China During 1978-2014, Environmental science & technology, 50, 13428-13435, 10.1021/acs.est.6b04308, 2016.

Xiao, M., Wang, Q., Qin, X., Yu, G., and Deng, C.: Composition, Sources, and Distribution of PM2.5 Saccharides in a Coastal Urban Site of China, Atmosphere, 9, 274, 10.3390/atmos9070274, 2018.

Xu, L. L., Chen, J. S., Yang, L. M., Niu, Z. C., Tong, L., Yin, L. Q., and Chen, Y. T.: Characteristics and sources of atmospheric mercury speciation in a coastal city, Xiamen, China, Chemosphere, 119, 530-539, 10.1016/j.chemosphere.2014.07.024, 2015.

Xu, X., Liao, Y., Cheng, I., and Zhang, L.: Potential sources and processes affecting speciated atmospheric mercury at Kejimkujik National Park, Canada: comparison of receptor models and data treatment

methods, Atmospheric Chemistry and Physics, 17, 1381-1400, 10.5194/acp-17-1381-2017, 2017.
Ye, Z., Mao, H., Lin, C. J., and Kim, S. Y.: Investigation of processes controlling summertime gaseous elemental mercury oxidation at midlatitudinal marine, coastal, and inland sites, Atmos. Chem. Phys., 16, 8461-8478, 10.5194/acp-16-8461-2016, 2016.
Zhang, L., Wang, S. X., Wang, L., and Hao, J. M.: Atmospheric mercury concentration and chemical speciation at a rural site in Beijing, China: implications of mercury emission sources, Atmospheric Chemistry and Physics, 13, 10505-10516, 10.5194/acp-13-10505-2013, 2013.
Zhang, Y., Yang, X., Brown, R., Yang, L. P., Morawska, L., Ristovski, Z., Fu, Q. Y., and Huang, C.: Shipping emissions and their impacts on air quality in China, Sci. Total Environ., 581, 186-198, 10.1016/j.scitotenv.2016.12.098, 2017.
Zhu, J., Wang, T., Talbot, R., Mao, H., Hall, C. B., Yang, X., Fu, C., Zhuang, B., Li, S., Han, Y., and Huang, X.: Characteristics of atmospheric Total Gaseous Mercury (TGM) observed in urban Nanjing, China, Atmospheric Chemistry and Physics, 12, 12103-12118, 10.5194/acp-12-12103-2012, 2012.
Zhu, J., Wang, T., Talbot, R., Mao, H., Yang, X., Fu, C., Sun, J., Zhuang, B., Li, S., Han, Y., and Xie, M.: Characteristics of atmospheric mercury deposition and size-fractionated particulate mercury in urban Nanjing, China, Atmospheric Chemistry and Physics, 14, 2233-2244, 10.5194/acp-14-2233-2014, 2014.
Zhu, J., Wang, T., Bieser, J., and Matthias, V.: Source attribution and process analysis for atmospheric mercury in eastern China simulated by CMAQ-Hg, Atmos. Chem. Phys., 15, 8767-8779, 10.5194/acp-15-8767-2015, 2015.
Zhu, W., Lin, C. J., Wang, X., Sommar, J., Fu, X., and Feng, X.: Global observations and modeling of atmosphere–surface exchange of elemental mercury: a critical review, Atmos. Chem. Phys., 16, 4451-4480, 10.5194/acp-16-4451-2016, 2016.

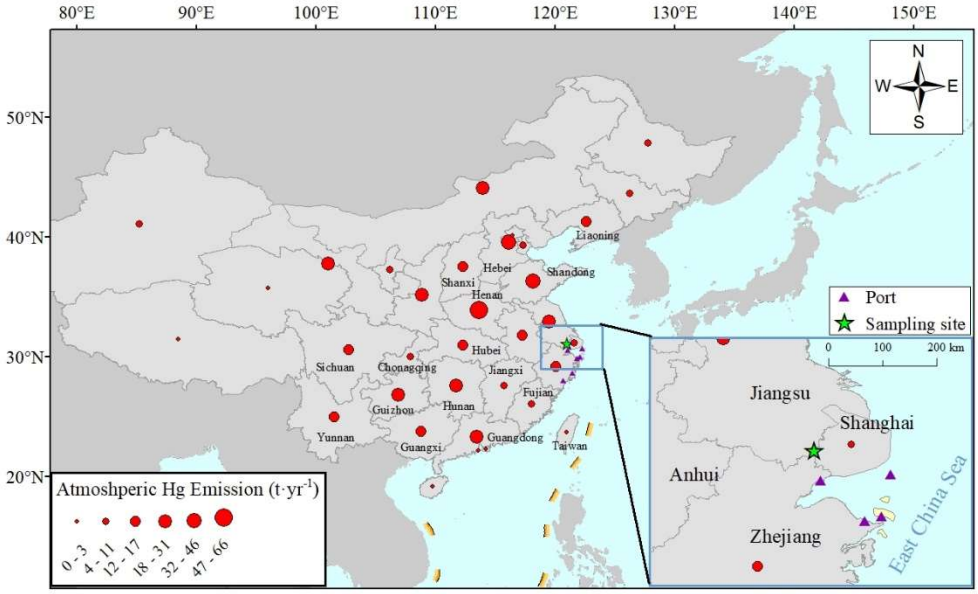

Figure 1. The location of the Dianshan Lake (DSL) site in Shanghai, China. The red dots in the map represent the anthropogenic atmospheric Hg emissions by each province in 2014 (Wu et al., 2016).

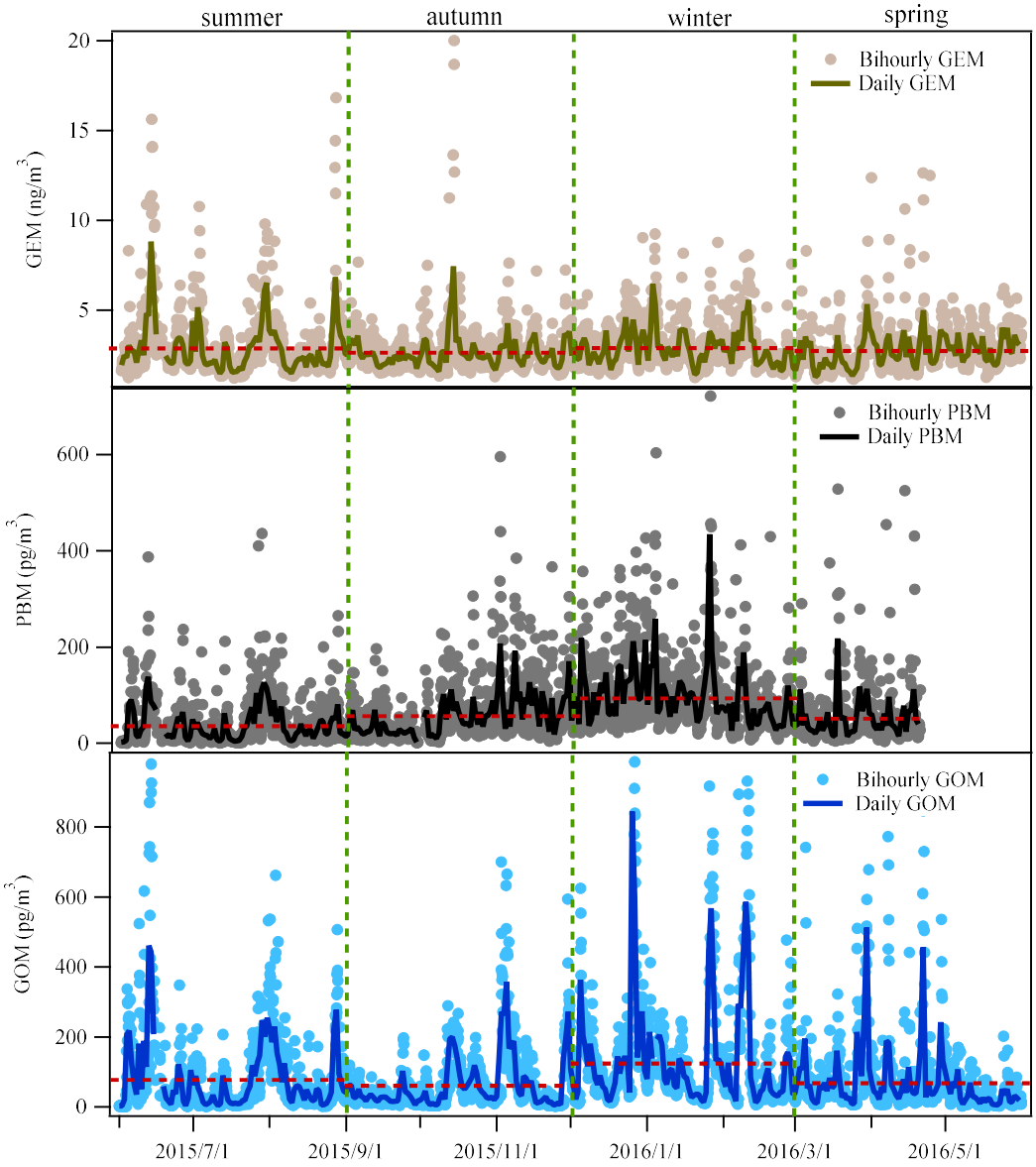

Figure 2. Time series of atmospheric Hg (GEM, PBM and GOM) concentrations during the whole study period at DSL. The red-dashed lines represent the mean concentrations of Hg species in each season.

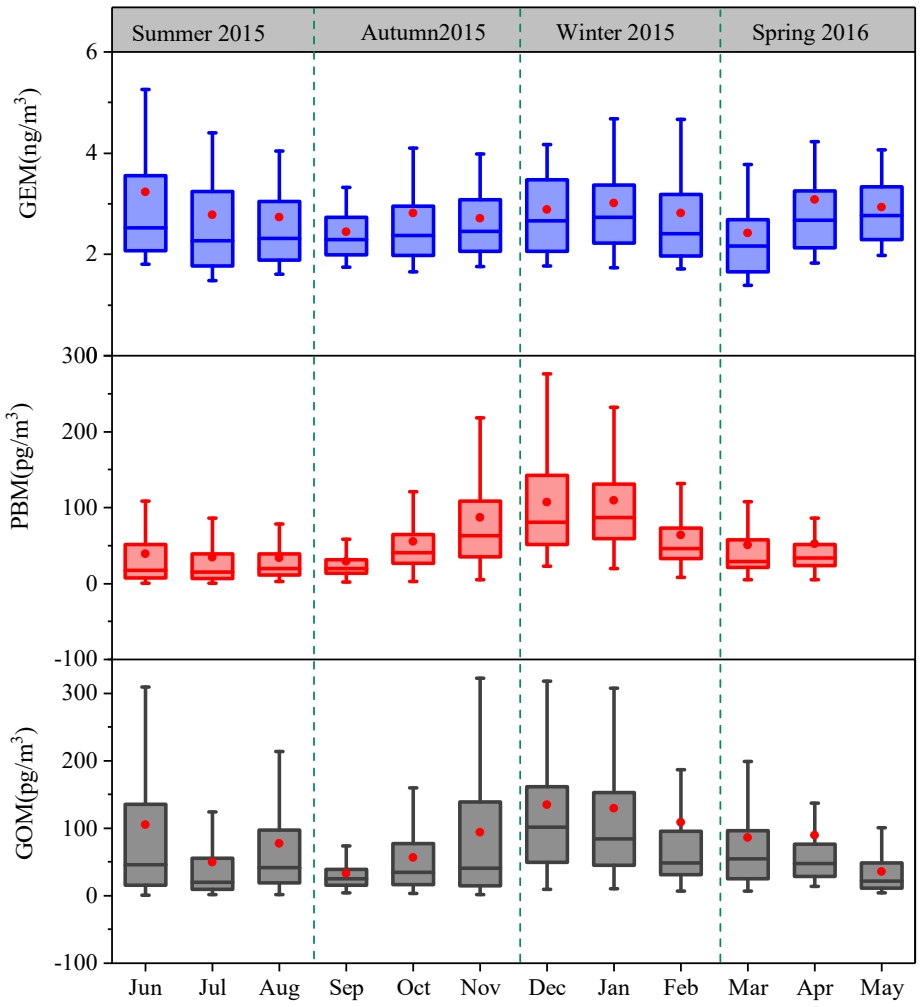

Figure 3. Monthly variation of GEM, PBM, and GOM concentrations. The 10th，25th, median, 75th and 90th percentile values are indicated in the box plots. The red dots represent the mean values.

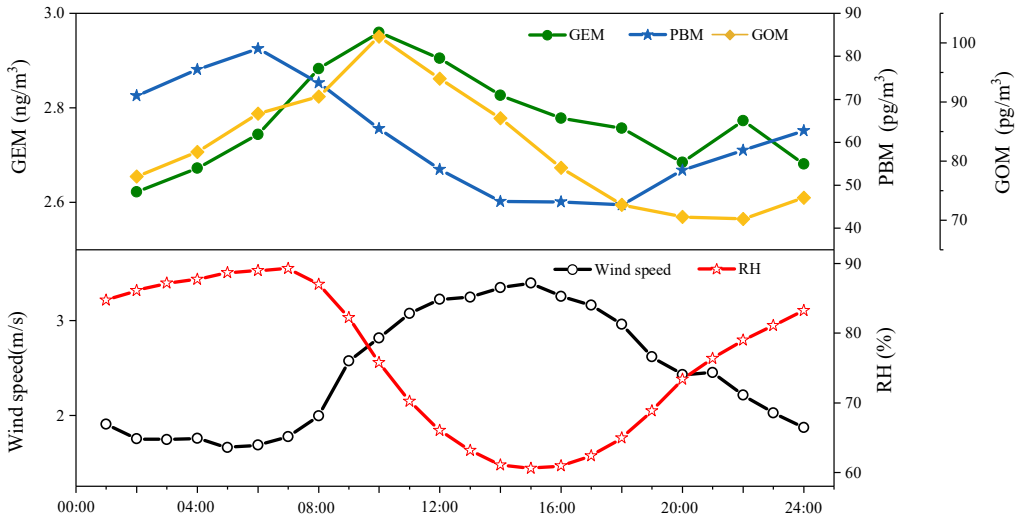

819

820

821 Figure 4. Annual mean diurnal variation of GEM, PBM, and GOM concentrations.

822

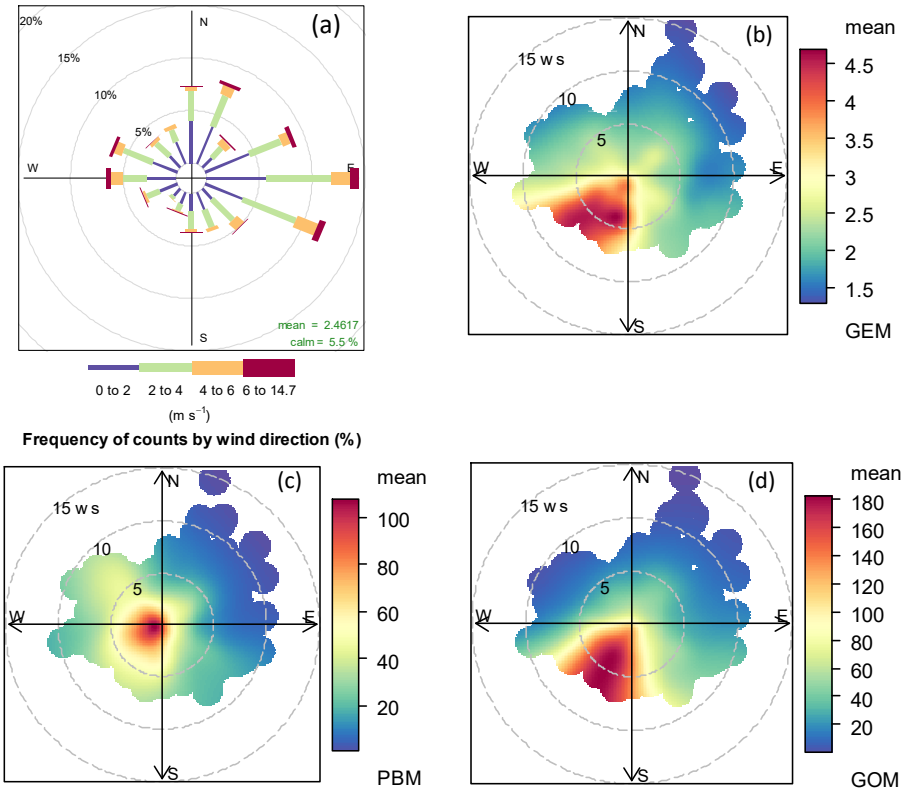

Figure 5. (a) Wind rose plot during the study period. Mean concentrations of (b) GEM, (c) PBM, and (d) GOM as a function of wind speed and wind directions. The radii of the circle in Figure 5 (a) represent the frequency of wind directions and the radii of the circle in Figure 5 (b), (c), and (d) represent the value of wind speed.

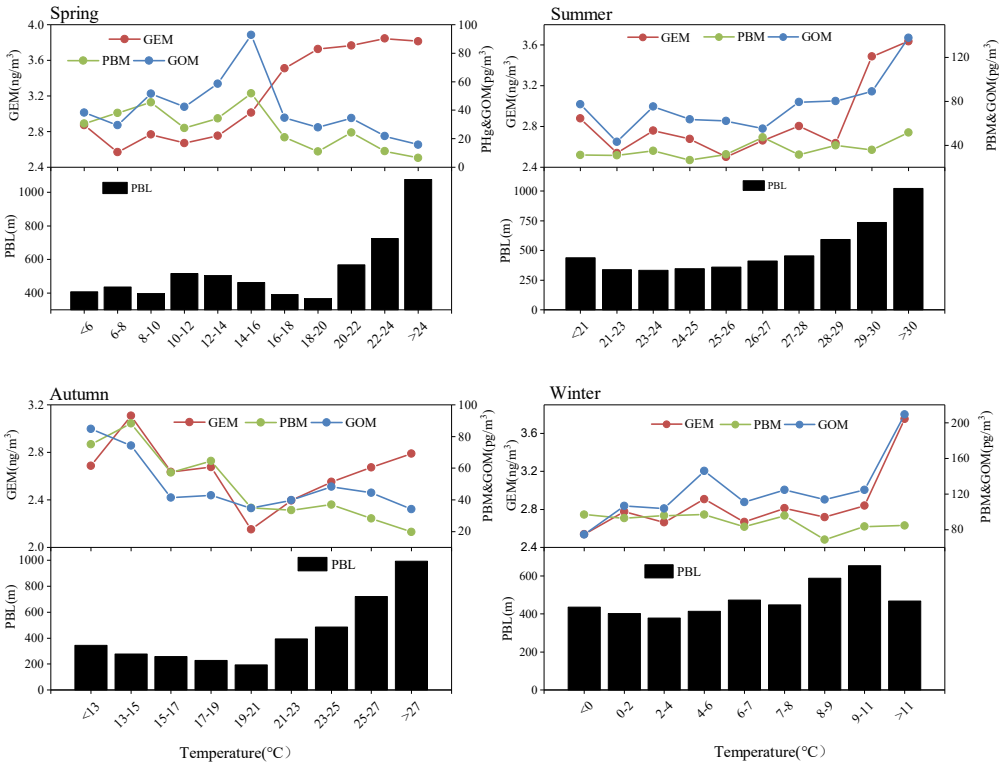

Figure 6. The variation of atmospheric Hg (GEM, PBM, and GOM) and PBL as a function of temperature in all four seasons.

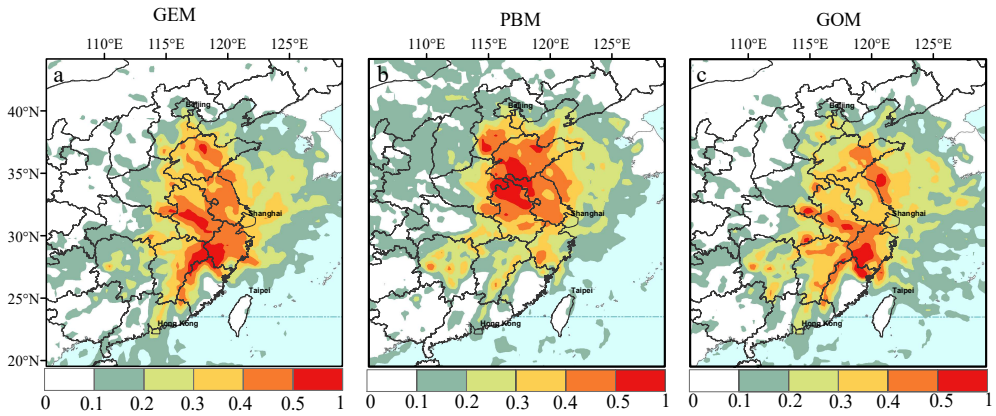

833

834 Figure 7. Potential source regions of atmospheric Hg (GEM, PBM, and GOM) at the observational
835 site according to PSCF analysis.

836

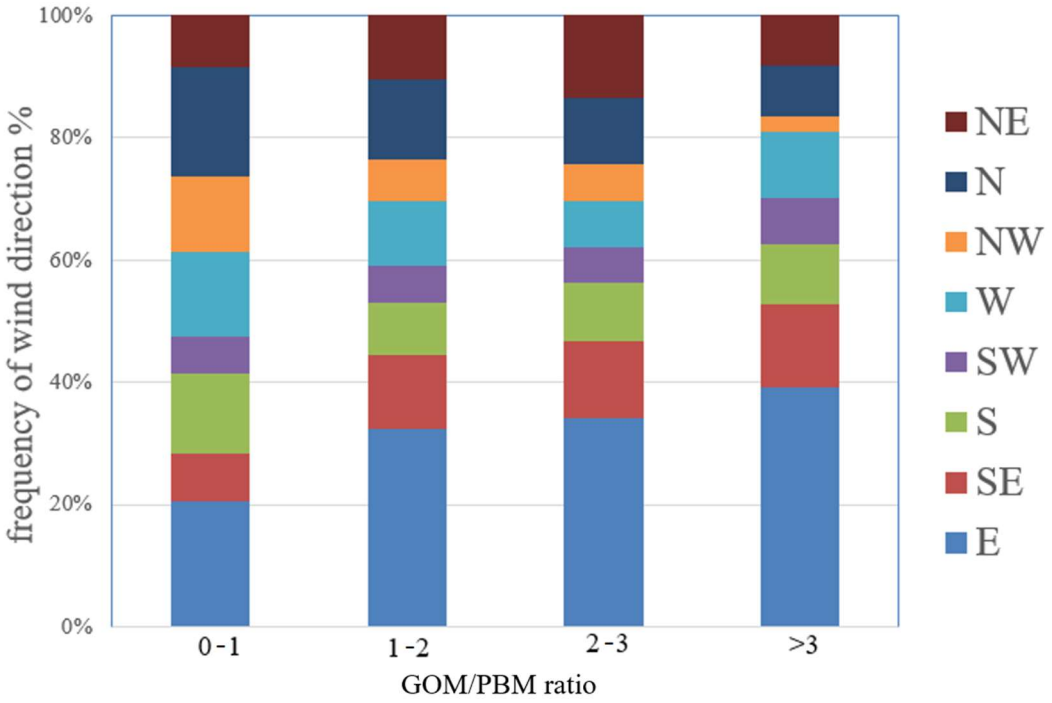

837

838 Figure 8. Frequency of wind directions under different ranges of GOM/PBM ratios.

839

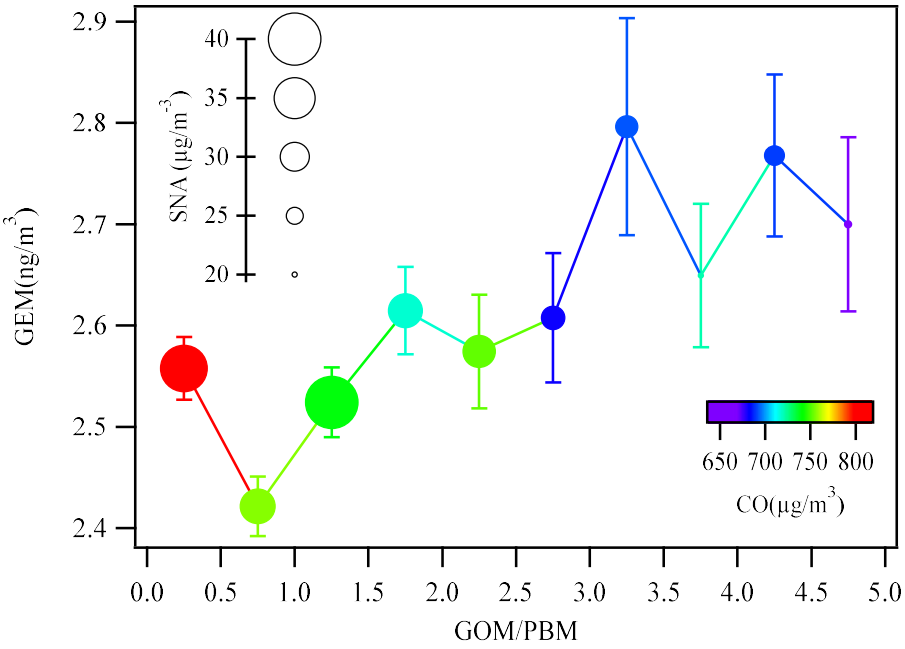

Figure 9. The GEM concentrations as a function of the GOM/PBM ratios in each bin of 0.5. The dots are colored by the concentrations of CO and the sizes of the dots represent the concentrations of SNA in $PM_{2.5}$. The bars represent one standard error of GEM concentration in each bin.

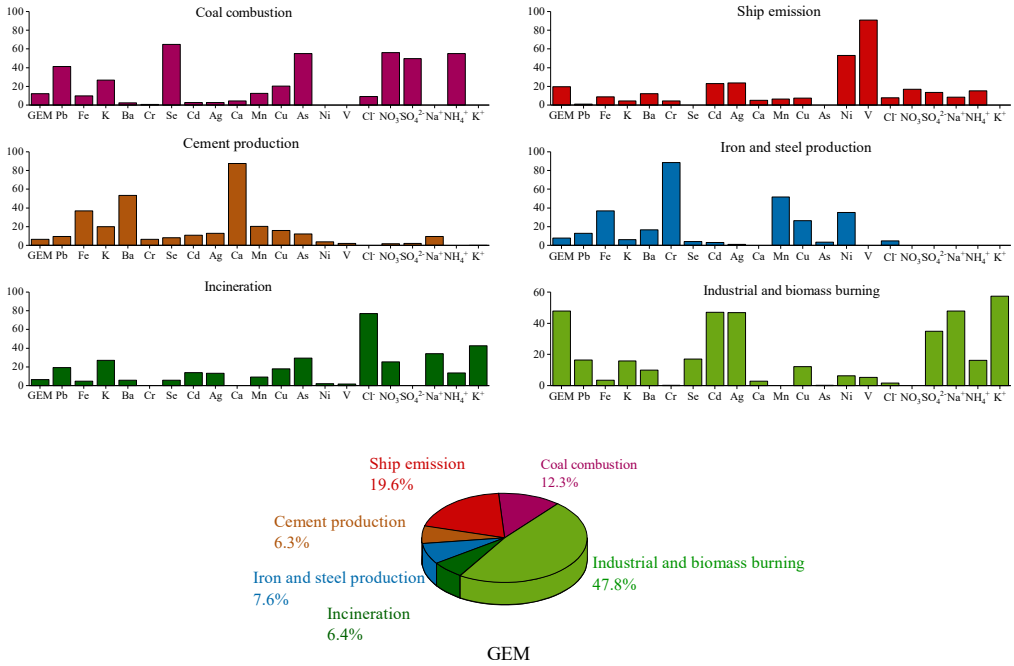

845

846 Figure 10. A six factor source apportionment for anthropogenic GEM based on PMF analysis.

847

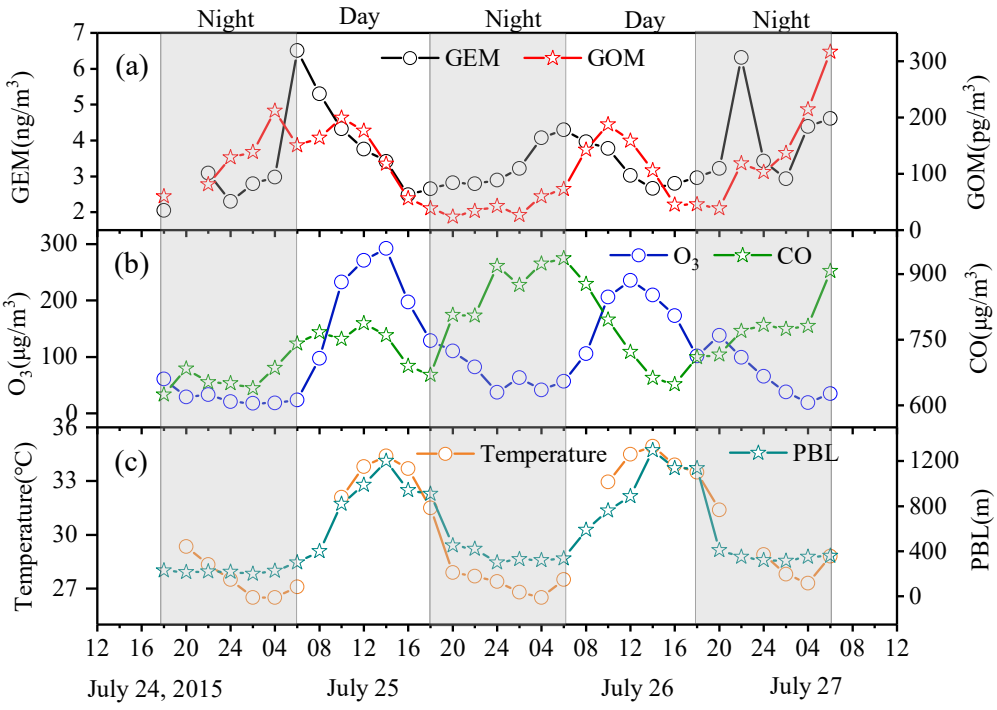

848

849 Figure 11. A case study of GEM oxidation from July 24 to 27, 2015. The time-series of GEM, GOM,
850 O_3, CO, temperature, and PBL are plotted. The shaded parts represent nighttime.

851

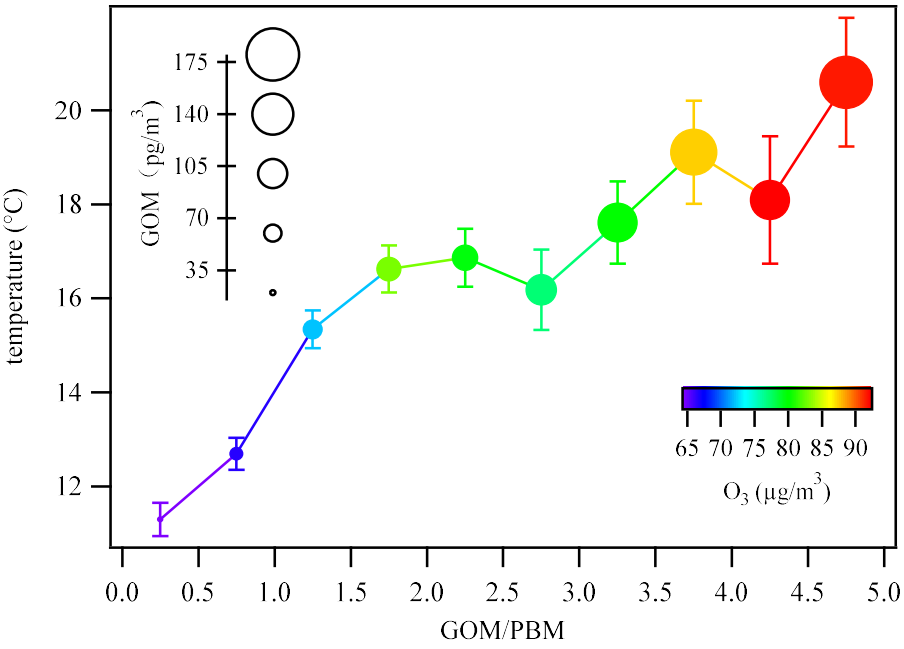

852

853 Figure 12. Temperature variations in each bin of the GOM/PBM ratios. The dots are colored by the
854 concentrations of O_3 and the sizes of the dots represent the concentrations of GOM. The bars
855 represent one standard error of temperature in each bin.

856

857

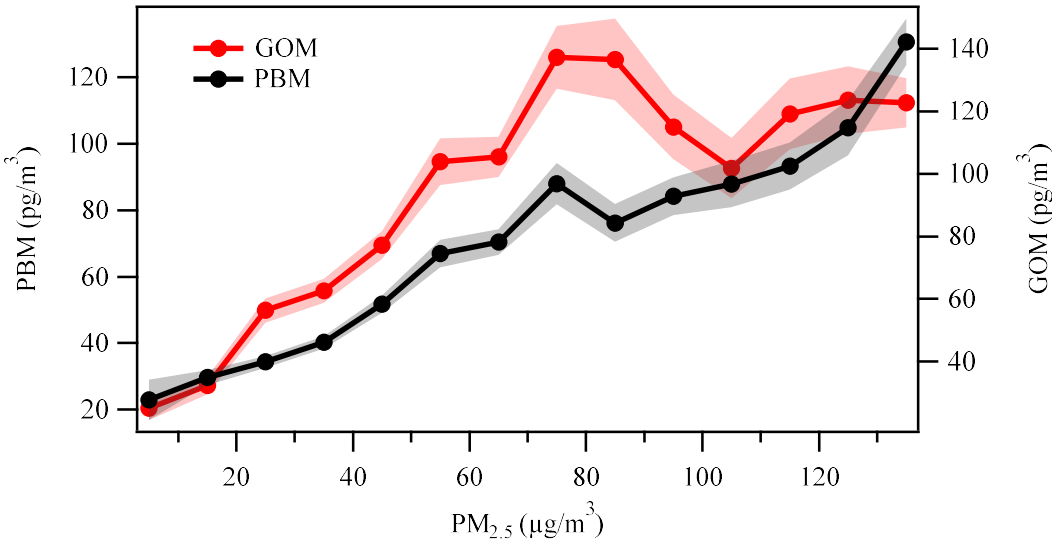

858

859 Figure 13. The variations of PBM and GOM as a function of $PM_{2.5}$ in each bin of 10 μg/m^3. The
860 shaded areas represent one standard error of GOM and PBM concentrations.

861

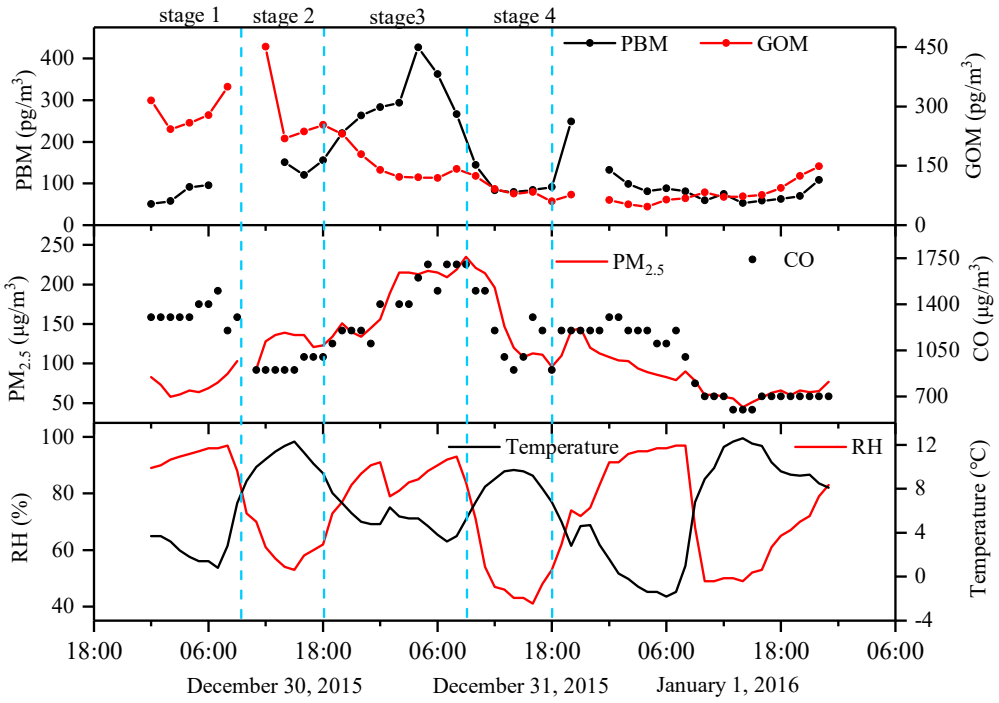

862

863 Figure 14. A case study of gas-particle portioning between GOM and PBM from December 30, 2015
864 to January 1, 2016, which was divided into different stages. The time-series of PBM, GOM, $PM_{2.5}$,
865 CO, temperature, and RH are plotted.

Table 1. The concentrations of speciated atmospheric mercury in this study and other sites around the world.

Location	Remarks	Year	GEM (ng/m^3)	PHg (pg/m^3)	RGM (pg/m^3)	Reference
Dianshan Lake Shanghai, China	Suburban	2015-2016	2.77±1.36	60.8±67.4	82.13±115.5	This study
Chongming Shanghai, China	Suburban	2009-2012	2.65±1.73	21.5±25.4	8.0±8.8	Zhang et al. (2017)
Xiamen, China	Suburban	2012-2013	3.5	174.41	61.05	Xu et al. (2015)
Guiyang, China	Urban	2009	9.72±10.2	368±676	35.7±43.9	Fu et al. (2011)
Miyun, China	Rural	2008-2009	3.23	98.2	10.1	Zhang et al. (2013)
Mt.Waliguan, China	Remote	2007-2008	1.98±0.98	19.4±18.1	7.4±4.8	Wan et al. (2009)
Seoul, Korea	Urban	2005-2006	3.22±2.10	23.9±19.6	27.2±19.3	Kim et al. (2009)
Nova Scotia, Canada	Rural	2010-2011	1.38±0.2	0.4±1.0	3.5±4.5	Cheng et al. (2014)
Elora,Ontario, Canada	Rural	2006-2007	1.17	16.40	15.1	Baya and Van Heyst (2010)
Chicago, USA	Urban	2007	2.5±1.5	9±20	17±87	Gratz et al. (2013)
Reno,USA	Suburban	2007-2009	2.0±0.7	7±7	18±22	Lyman and Gustin (2009)
Rochester, NY, USA	Urban	2008-2009	1.49	6.57	4.08	Huang et al. (2010)

Table 2. PCA (Principal Component Analysis) analysis for GEM at DSL.

	Factor 1	Factor 2	Factor 3	Factor 4
GEM	0.50	0.25	0.11	0.07
SO_2	**0.69**	-0.20	-0.18	0.35
NO_2	0.38	-0.49	0.35	0.39
SO_4^{2-}	**0.84**	0.13	0.15	0.00
NH_4^+	**0.88**	-0.12	0.18	0.07
K^+	**0.77**	-0.25	0.04	0.39
Pb	**0.80**	-0.17	0.04	0.32
Se	**0.87**	-0.05	0.01	0.29
As	**0.82**	-0.23	0.06	0.33
O_3	0.06	**0.79**	-0.30	0.03
NH_3	0.03	**0.73**	0.36	-0.04
Temperature	-0.23	**0.82**	0.17	-0.03
Ni	0.24	-0.02	**0.85**	0.22
V	-0.03	0.11	**0.90**	-0.05
Fe	0.50	-0.12	0.24	**0.74**
Ca	0.26	0.08	0.00	**0.90**
Explained variance %	34.15	14.85	13.43	12.89